

In-situ SnSe deposition as passivation for scalable and stable quasi-2D lead-tin perovskite solar cells

Lijun Chen,^a Eelco Kinsa Tekelenburg,^a Kushagra Gahlot,^a Matteo Pitaro,^a Jun Xi,^b Alessia Lasorsa,^a Giovanna Feraco,^a Loredana Protesescu,^a Patrick C. A. van der Wel,^a Giuseppe Portale,^a Petra Rudolf,^a Christoph J Brabec,^{a,c} and Maria Antonietta Loi ^{*a}

Lead-tin (Pb-Sn) perovskites are a highly promising composition for single-junction and all-perovskite tandem solar cells due to their narrower bandgap and reduced toxicity. While the use of quasi-two-dimensional (quasi-2D) Ruddlesden-Popper phases has resulted in superior stability towards the environment and large improvement in the crystallization with respect to the 3D compositions, very little work has been done towards their deposition with scalable techniques. Here, $\text{PEA}_2(\text{FA}_{0.5}\text{MA}_{0.5})_4(\text{Pb}_{0.5}\text{Sn}_{0.5})_{n+1}\text{I}_{3n+4}$ ($n=5$) with a gradient structure is successfully prepared for the first time by a two-step blade coating. Perovskite films which are treated with tin (II) acetate (SnAc_2) along with N, N-dimethylselenourea (DMS) exhibit a reduced number of surface traps and enhanced surface crystallization, owing to the in-situ formation of tin selenide (SnSe). Record devices with power conversion efficiency (PCE) of 15.06%, an open circuit voltage (V_{oc}) of 0.855 V, and negligible hysteresis are obtained. More importantly, the hydrophobic SnSe significantly protects the active layer from the environment. These devices retain 91% of the original PCE after 10 days in ambient air (30%-40% humidity) without encapsulation, and nearly no-degradation of the PCE is detected after over a month of storage in inert atmosphere, and under continuous MPP tracking for 15 hours.

Introduction

Single-junction Pb-based perovskite solar cells (PSCs) have been extensively investigated in the last years and recently a certified record PCE of 25.7% has been reported.¹ However, the road towards commercialization require efforts on improving device stability and on developing scalable deposition techniques. Mixed Pb-Sn perovskites show a reduced toxicity with respect to pure

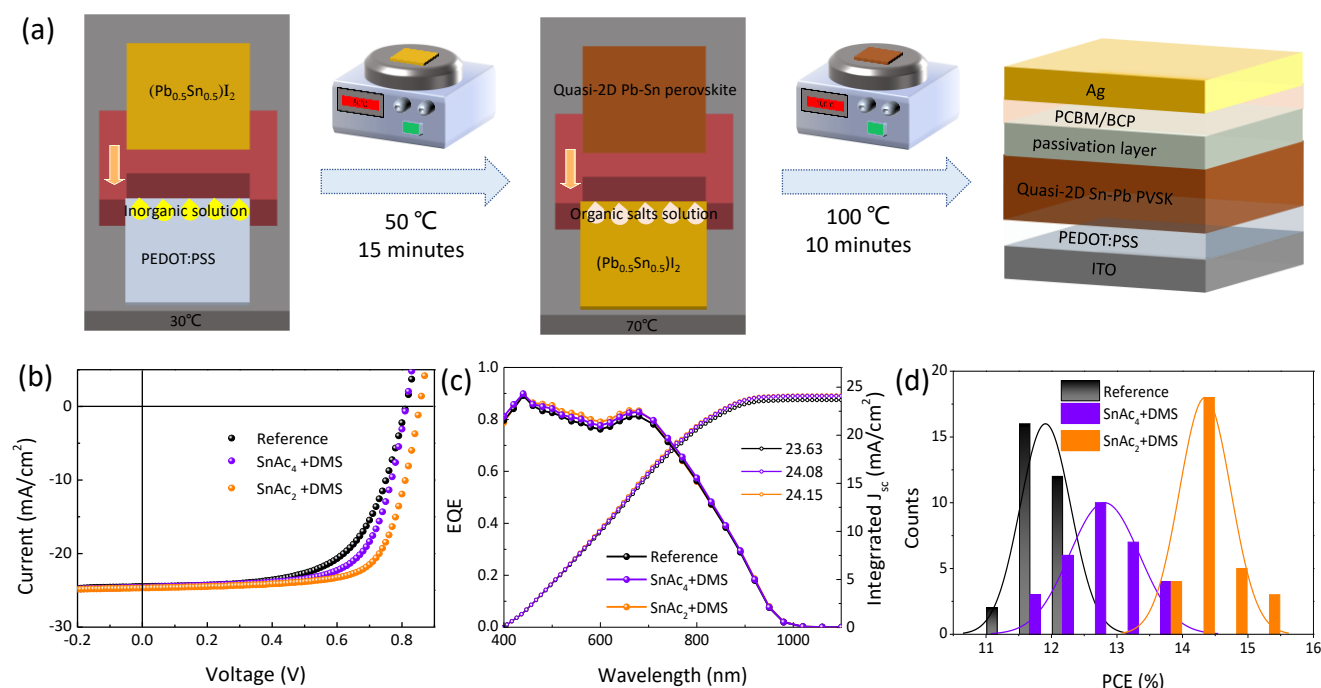


Figure 1 (a) Schematic diagram of the preparation of quasi-2D Pb-Sn perovskite with a two-steps blade coating process. (b) J-V curves of the best-performing PSCs. (c) EQE spectra and integrated photocurrent of the devices. (d) Statistical distribution of PCEs for the three different samples type.

Pb one,² but also a narrower bandgap (1.2-1.3 eV). For these reasons, Pb-Sn alloys are one of the ideal candidates as light absorbers, which show great potential not only for single-junction solar cells but also for all-perovskite tandem devices,^{3,4} as illustrated by the recently reported certified efficiency of 26.4%.⁵ Lately, a variety of efforts including interface passivation and improved crystallization have been devoted to reduce p-type doping and non-radiative recombination, resulting in record efficiencies (>23%).^{6,7} However, Pb-Sn devices are still characterized by inferior stability with respect to the Pb counterpart,⁸⁻¹⁶ and the environmental sensitivity of Pb-Sn perovskites is considered one of the primary obstacles that limits their further development.¹⁷⁻²⁰

One of the most successful strategies to enhance the environmental stability of metal halide perovskites has been the fabrication of quasi-2D systems.²¹⁻²⁴ By introducing large organic spacer cations, such as aliphatic or aromatic mono ammonium, diammonium, and triammonium cations,^{10,25-29} low dimensional systems where layers of inorganic octahedra are separated by the spacer cations are formed. The long organic cations have also been demonstrated to induce preferential crystal orientation by tuning the nucleation,^{30,31} and determining a lower trap density.³²⁻³⁴ The presence of organic cations on the surface and grain boundaries, not only protects the inorganic layers from moisture, but also improves their structural stability.^{35,36} Quasi-2D Ruddlesden-Popper (RP) Pb-Sn perovskites in principle should combine the excellent photovoltaic characteristics of Pb-Sn perovskites with the robust environmental properties of 2D RP systems. However, quasi-2D Pb-Sn perovskites solar cells are rarely reported in literature, and more related reports are inclined to use a limited amount of long organic cations as nucleation agents. This may be due to the difficulties pertaining to vertical growth of low-dimensional phases and the competitive crystallization kinetics between Pb and Sn sublattices. The state-of-the-art PCE of quasi-2D Pb-Sn devices is only about 10%,³⁷⁻³⁹ (see Table 1) but it is interesting to note that these devices show better stability towards the environment compared to 3D counterparts. Therefore, it is important to improve the PCE of such devices as they may help in obtaining the high stability required for applications.

Most of the Sn-Pb perovskite solar cells reported up until now were obtained using spin-coating, which is a wasteful technique with precursor utilization rate limited to only 5%-10%. This technique, while used in semiconductor industry at the wafer size, it is not compatible with solar module production. Recently, our group proposed a scalable technique involving a 2D perovskite-template driven growth of 3D Pb-Sn perovskites, where the champion device exhibits a PCE of 9.77% limited by the formation of cracks in the conversion process.⁴⁰ It is important to note that in this case no special treatments were performed to suppress surface traps, while it is well accepted that surface traps at the interface with electron or hole transport layers play an important role in nonradiative recombination, which affects both device efficiency and stability.⁴¹⁻⁴⁵

Blade coating is a facile method that has a very high precursor utilization rate and allows tuning of the deposition temperature. Importantly, there are a few industrial-scale techniques which have similar characteristics as of blade coating, making possible an almost immediate transfer of the deposition conditions. In this work, a quasi-2D Pb-Sn perovskite of $\text{PEA}_2(\text{FA}_{0.5}\text{MA}_{0.5})_4(\text{Pb}_{0.5}\text{Sn}_{0.5})_5\text{I}_{16}$ (PEA= phenethylammonium, FA= formamidinium, MA= methylammonium) with gradient structure is successfully prepared for the first time with a two-step blade coating process. This technique allows for controlling the growth of perovskite with low temperature manipulation, giving rise to a reference device of PCE of 12.42%. However, great attention should be given to surface passivation to reduce nonradiative recombination and improve photovoltaic performance. Inspired by the attractive physical properties of SnSe, a surface treatment using SnAc_2 +DMS is applied on the quasi-2D perovskite surface. The in-situ synthesized SnSe obtained from the reaction of SnAc_2 and DMS significantly reduces nonradiative recombination and suppresses ion migration. As a result, we fabricated quasi-2D Pb-Sn perovskite solar cells with scalable deposition technique, showing a champion PCE of 15.06% and a V_{OC} of 0.855 V. These optimized devices retain 91% of the original PCE after 10 days of storage in ambient conditions (30%-40% humidity) without encapsulation and show nearly no-degradation of the PCE when stored

Table 1 Photovoltaic parameters of quasi-2D Pb-Sn perovskite solar devices as reported in literature compared to this work.

Perovskites	V_{OC} (V)	J_{SC} (mA/cm ²)	FF (%)	PCE (%)	Fabrication methods	Reference
$(\text{BA})_2(\text{MA})_3\text{Pb}_3\text{SnI}_{13}$	0.80	12.05	61.81	5.96	Spin coating	[37]
$(\text{BA}_2\text{MA}_3\text{Pb}_4\text{I}_{13})_{0.6}$ $(\text{PEA}_2\text{FA}_3\text{Sn}_4\text{I}_{13})_{0.4}$	0.808	17.39	71.24	10.013	Spin coating	[38]
$(\text{t-BA})_2(\text{FA}_{0.85}\text{Cs}_{0.15})_4$ $(\text{Pb}_{0.6}\text{Sn}_{0.4})_5\text{I}_{16}$	0.70	24.2	63	10.6	Spin coating	[39]
$\text{PEA}_2(\text{FA}_{0.5}\text{MA}_{0.5})_4$ $(\text{Pb}_{0.5}\text{Sn}_{0.5})_5\text{I}_{16}$	0.855	24.67	71	15.06	Blade coating	This work

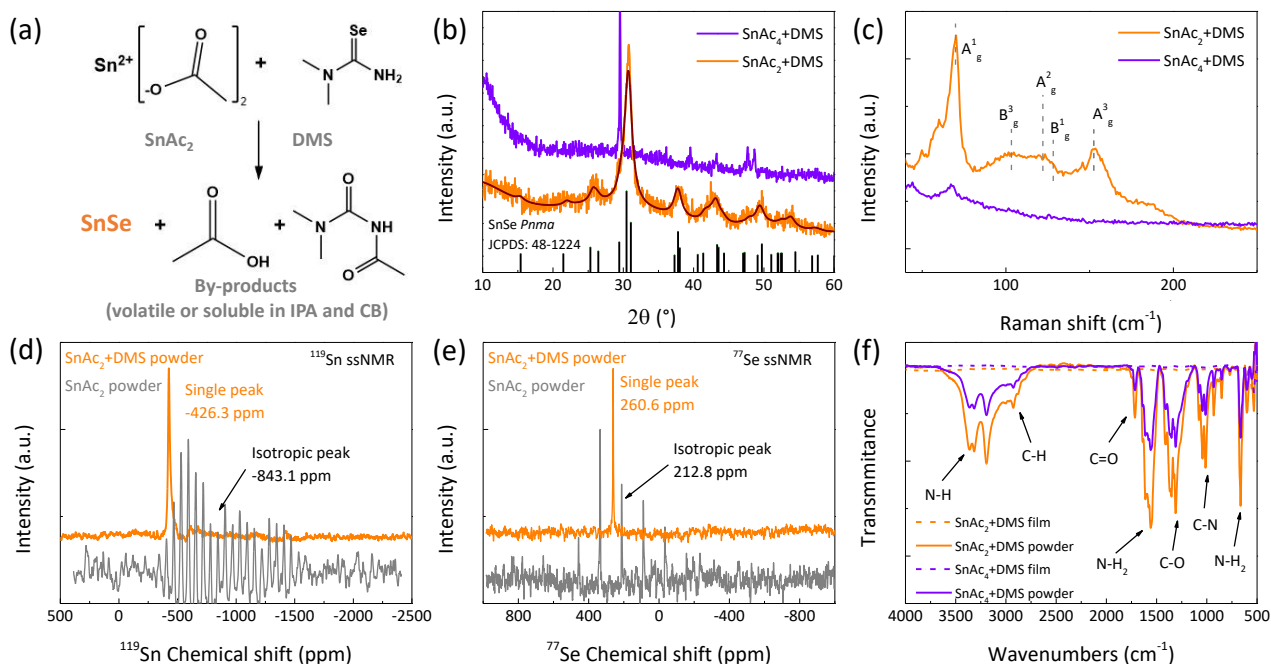


Figure 2 (a) The reaction scheme of SnAc_2 and DMS yielding SnSe and by-products (acetic acid and acetamide derivative). (b) Powder XRD patterns of the products between SnAc_4 , SnAc_2 and DMS via thin films procedure after annealing; in black the SnSe Pnma reference is displayed. (c) Raman spectra of the SnAc_2+DMS and SnAc_4+DMS thin films annealed after annealing. (d) ^{119}Sn ssNMR spectra of SnAc_2 precursor (grey) and SnAc_2+DMS solid state traction products (orange), showing a change in the isotropic shift (marked with arrows) and MAS side band patterns (see Figure S6 a-d). (e) ^{77}Se ssNMR spectra of DMS precursor (grey) and SnAc_2+DMS solid state traction products (orange) (see Figure S7 a-b). (f) FTIR spectra of SnAc_2+DMS and SnAc_4+DMS powders, and their corresponding films after thermal annealing.

in a glovebox for over 1 month, or under continuous MPP tracking for 15 h. This are highly significant improvements when compared with the stability performance of the reference device without any surface passivation.

Results and discussion

Figure 1a shows the schematic of the two-step blade coating process. In the first step, the inorganic $(\text{Pb}_{0.5}\text{Sn}_{0.5})\text{I}_2$ film is deposited on the substrate kept at 30 °C, followed by an annealing step at 50 °C. Then, the solution of organic salts including PEAI, FAI, MAI, and MACl are deposited on top to allow their diffusion throughout the inorganic layer of $(\text{Pb}_{0.5}\text{Sn}_{0.5})\text{I}_2$ to form a quasi-2D Pb-Sn perovskite. Ultraviolet photoelectron spectroscopy (UPS) and UV-vis absorption spectra reveal that we obtained a perovskite with an ideal bandgap (~1.3 eV) and suitable valence/conduction band (4.31 eV and 5.61 eV), as illustrated in Figure S1 and Figure S2.

Devices of structure ITO/PEDOT:PSS/Quasi-2D Pb-Sn PVSK/PCBM/BCP/Ag fabricated in this way show a record efficiency of 12.42%, with relatively limited V_{OC} (0.812 V) and FF (62%), as shown in **Figure 1b**. To improve the photovoltaic performances, we investigate the SnAc_4 and SnAc_2 as possible passivation agents on the perovskite surface, enabling a slight improvement on the V_{OC} and FF (Figure S3a and Table S1). We further investigate the possibility of passivating the surface traps by depositing DMS with SnAc_4 and SnAc_2 , respectively. Interestingly, after surface treatment with SnAc_4+DMS , a higher PCE of 13.65% with an improved FF of 68% is achieved due to the possible passivation provided by carbonyl (C=O) and -NH₂ groups. A champion PCE of 15.06% (hysteresis index (HI) of 0.26%) with a much-improved V_{OC} (0.855 V) and FF (71%) is obtained with a SnAc_2+DMS (0.001 M) treatment (Figure S3b and Table S2). We expect that the in-situ reaction give rise to the formation of an ultrathin SnSe passivation layer.

It is important to underline that these devices show excellent area scalability, with devices of 0.81 cm² exhibiting a PCE of 11.31% (Figure S3c and Table S3), indicating that this strategy is very promising for scalable fabrication of efficient PSCs. **Figure 1c** shows external quantum efficiency (EQE) spectra with integrated J_{SC} of 23.63, 24.08, and 24.15 mA/cm² for the reference and optimized devices, respectively. All values agree well with their corresponding J_{SC} in the J-V characteristics. And we can see an improvement in EQE spectra after surface passivation in the range between 400-700 nm rather than whole wavelength. The minimal inconsistent between UV-vis absorption spectra and EQE is due to differences in extraction of carriers generated by incident photons of different energy. **Figure 1d** and S4 show the results obtained from the characterization of 30 solar cells for each configuration to confirm the reproducibility of the fabrication and surface treatment, the average PCE is improved from 11.91% (reference) to 12.81% (SnAc_4+DMS) and 14.33% (SnAc_2+DMS) mainly owing to the large improvement of average V_{OC} and FF.

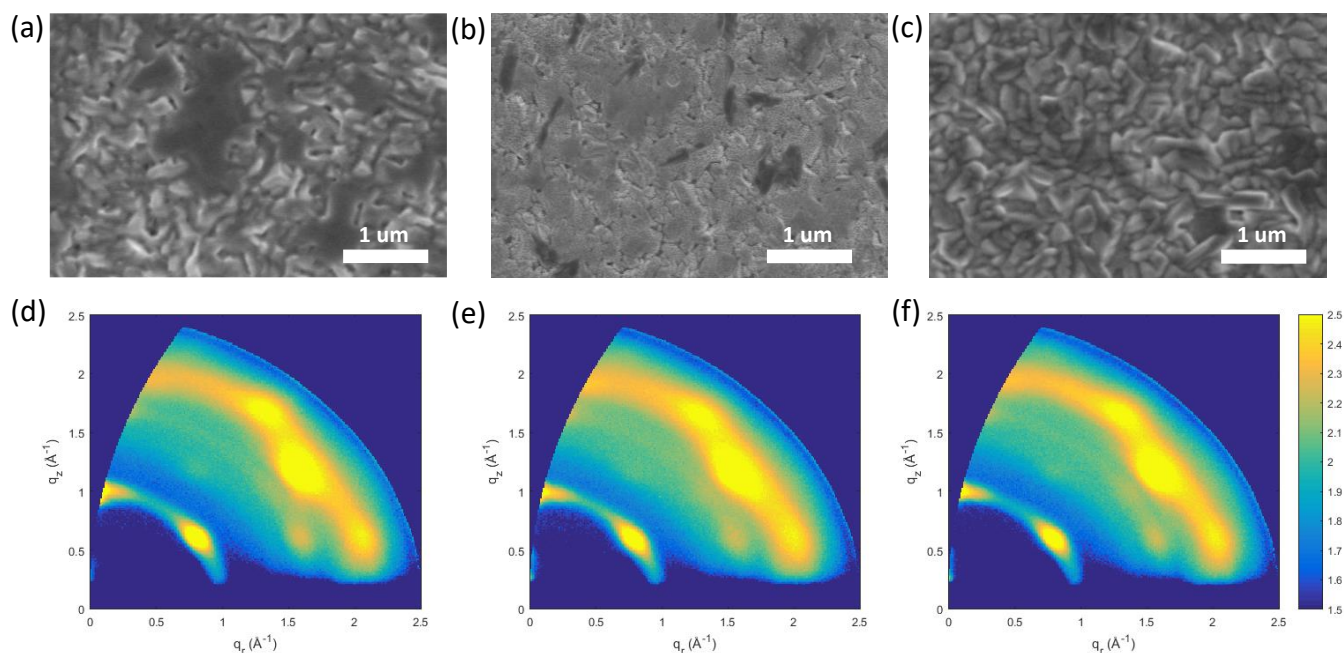


Figure 3 SEM micrographs of the reference perovskite film (a) and of the samples treated with SnAc₄+DMS (b) and SnAc₂+DMS (c). (d-f) GIWAXS patterns of the corresponding three different perovskite films recorded using an incident angle of 0.5°.

As mentioned, we propose that the origin of these large improvements in the solar cell performance is due to the in-situ formation of SnSe on the perovskite surface. To prove the formation of SnSe we conducted control solid state (solvent free) reactions of the precursors at different temperatures (see Figure S5). DMS reacts strongly with the SnAc₂ in a solvent free system at a temperature of 60 °C, where the colour of the reaction mixture changed from white to black. This is in stark contrast to either SnAc₄ or SnI₂ solid state reactions with DMS that did not show any variation of colour, indicating that the reactivity of SnAc₂ with DMS to yield SnSe at low temperature is more favourable compared to the other Sn-based precursors. The reaction scheme for the synthesis of SnSe from SnAc₂ and DMS is displayed in the **Figure 2a**. The resulting by-products are volatile at the annealing temperature (acetic acid) or soluble in the solvent used to process the thin-film (acetamide-derivate). For further characterization, we used annealed thin films (80 °C) obtained from precursors dispersed in a mixture of isopropanol (IPA) and chlorobenzene (CB) and solid-state powder reaction (ball-milling). To demonstrate the formation of SnSe from the SnAc₂+DMS and SnAc₄+DMS mixtures, powder X-ray diffraction (XRD) measurements were carried out on the thin films and reported in **Figure 2b**. The fitted diffraction peaks of SnAc₂+DMS are assigned to (201), (111), (311), (411) and (511) planes, (JCPDF 48-1224) corresponding to SnSe orthorhombic (Pnma). The SnAc₄ and DMS mixture did not yield any crystalline SnSe product. The formation of SnSe, was also confirmed by the Raman spectra (**Figure 2c**), where the five vibration modes at 70 cm⁻¹ (A¹_g), 102 cm⁻¹ (B³_g), 120-130 cm⁻¹ (band overlapping between A¹_g and B¹_g), and 152 cm⁻¹ (A³_g) are present, which is consistent with previously published data.⁴⁶ The vibrations for the SnAc₄+DMS mixture are very weak, confirming that the formation of SnSe is only favourable from SnAc₂, namely for Sn²⁺ containing precursors, as expected. Interesting, the SnSe powders obtained from solid-solid reaction are not very soluble in a mixture of IPA and CB (1:1 volume ratio) with a concentration of 1mM, and when the solution is used as passivation, devices exhibit poor performance with PCE of 10.10% (see Figure S5b and S5c). This results further underline the importance of the in-situ deposited SnSe.

X-ray photoelectron spectroscopy (XPS) measurements were conducted on the quasi-2D Pb-Sn perovskite films with and without SnAc₂+DMS/SnAc₄+DMS to further elucidate the in-situ deposition of SnSe (see details in Figure S6). Moreover, we performed magic-angle-spinning (MAS) solid-state nuclear magnetic resonance (ssNMR) spectroscopy on the solid-state mixture and its precursors (**Figure 2 d and e**; Figure S7-S9). In the ¹¹⁹Sn ssNMR MAS spectrum, the SnAc₂ precursor showed an isotropic peak at -843.1 ppm (gray spectrum, **Figure 2d**), whereas the SnSe final reaction product displayed an isotropic peak at -426.2 ppm, indicating the complete reaction of SnAc₂ even in the solid-state procedure. Figure S8 shows the ¹¹⁹Sn NMR spectrum from 5000 ppm to -5000 ppm, with no peaks from side products or residual precursors. The ⁷⁷Se ssNMR spectra (**Figure 2e**) showed an isotropic peak at 212.8 ppm for the DMS (gray spectrum) and a single peak at 260.6 ppm for the SnSe (orange spectrum). The complete ¹¹⁹Sn and ⁷⁷Se ssNMR investigation for the precursors and final products are presented in Figures S7-S9. Both solid-state reactions and the thin films deposition were investigated with Fourier-transform infrared spectroscopy (FTIR). We noticed that for

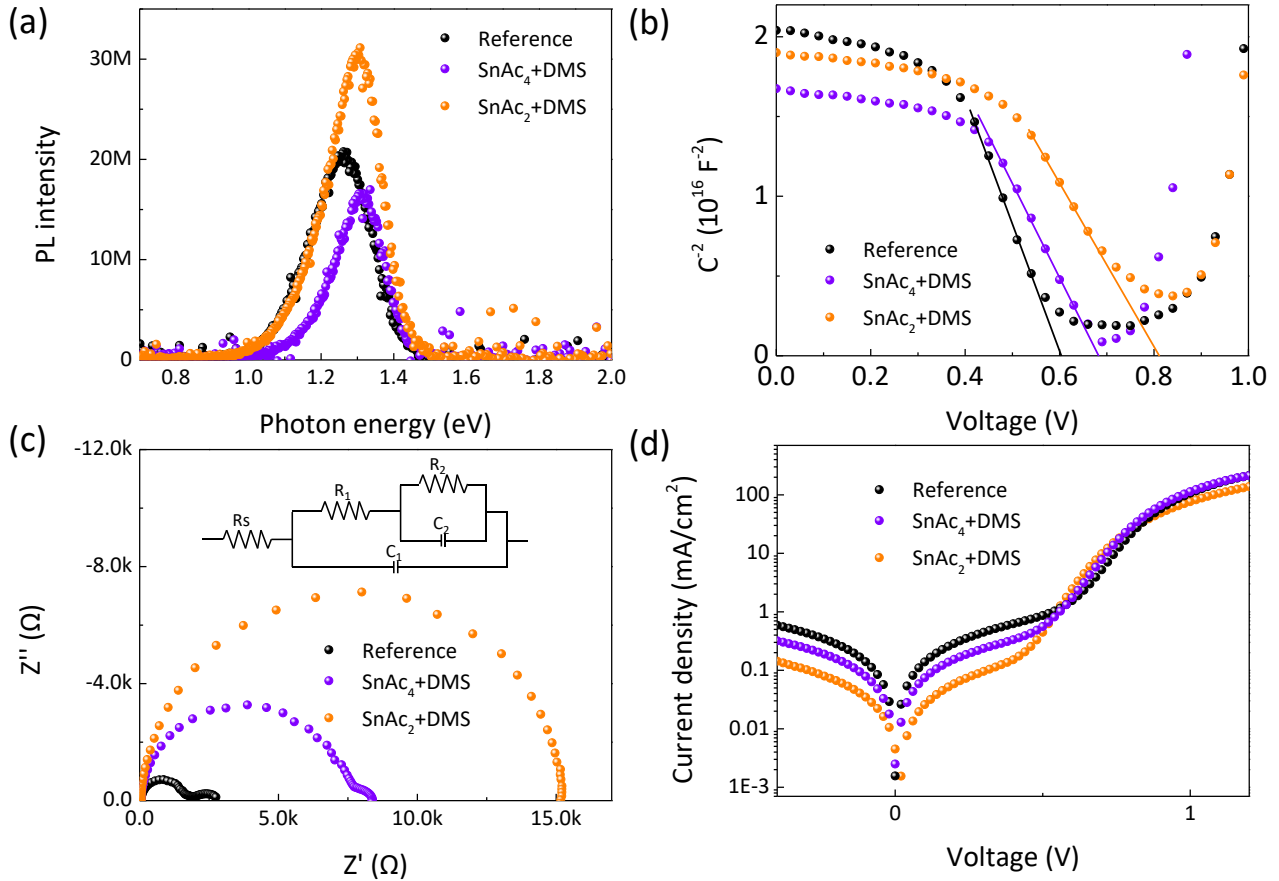


Figure 4 (a) Steady-state PL curves of the reference and optimized perovskite films. (b) Mott-Schottky plots analysis of the devices with and without surface treatment. (c) EIS spectra measured in dark for the three different samples, the insert shows the equivalent circuit used for the fitting. (d) The dark J-V curves of three corresponding devices.

the solid-state reactions, the vibrations corresponding to the by-products (acetic acid and the acetamide derivate) are present (**Figure 2f**, solid lines), indicated by the functional groups of N-H stretching vibrations ($\sim 3315\text{--}3160\text{ cm}^{-1}$), C-H symmetric stretching vibrations ($\sim 2930\text{ cm}^{-1}$), C=O stretching vibrations ($\sim 1714\text{ cm}^{-1}$), N-H₂ scissoring ($\sim 1555\text{ cm}^{-1}$), C-O stretching vibrations ($\sim 1310\text{ cm}^{-1}$), C-N stretching vibrations ($\sim 1014\text{ cm}^{-1}$), and N-H₂ wagging ($\sim 665\text{ cm}^{-1}$). But when the thin film procedure was performed, no vibration corresponding to the by-products was observed in the mid-IR region. This is due to the solubility and volatility of the by-products, allowing for an efficient solvent and temperature removal from the film surface. SnSe exhibits suitable band gap (1.3 eV), high absorption coefficient (10^5 cm^{-1}), and high chemical stability,⁴⁷ which gives indication that it may have broad application prospects in photovoltaic devices. It is important to underline that this passivation strategy based on SnSe is reported here for the first time.

To better understand the impact of the surface treatment on the morphology, scanning electron microscopy (SEM) and atomic force microscopy (AFM) measurements were conducted. As shown in **Figure 3a-c** and **Figure S910**, for the SEM and AFM, respectively, the reference sample shows irregularly distributed pinholes and voids, which are known to be accompanied by surface traps.⁴⁸ The large darker substance appearing in the SEM micrographs corresponds to low-n phases, while the bright signals are attributed to excess PbI₂/SnI₂. Here, it is important to remember that the sample is fabricated with a two-step process, which easily give rise to stoichiometric variations along the direction perpendicular to the substrate. For the SnAc₄+DMS treated sample, we observe that the surface is evenly covered with a layer of very small particles, which we expect to originate from the unreacted SnAc₄+DMS. This hypothesis is consistent with the results of both the Raman and XRD measurements. However, the SnAc₄+DMS treated sample shows a dense coverage of the perovskite surface with fewer pinholes and remaining impurities, this seems in agreement with the reported device performance improvement. Interestingly the surface treatment performed with SnAc₂+DMS, gives rise to films of uniform surface coverage and densely packed grains without pinholes and voids. Moreover, the reduced amount of the bright signals suggests a possible reduction of the presence of PbI₂/SnI₂ on the surface, which will be confirmed below by GIWAXS measurements. The AFM images of the three perovskite films present similar surface morphologies as the SEMs micrographs (**Figure S10**).

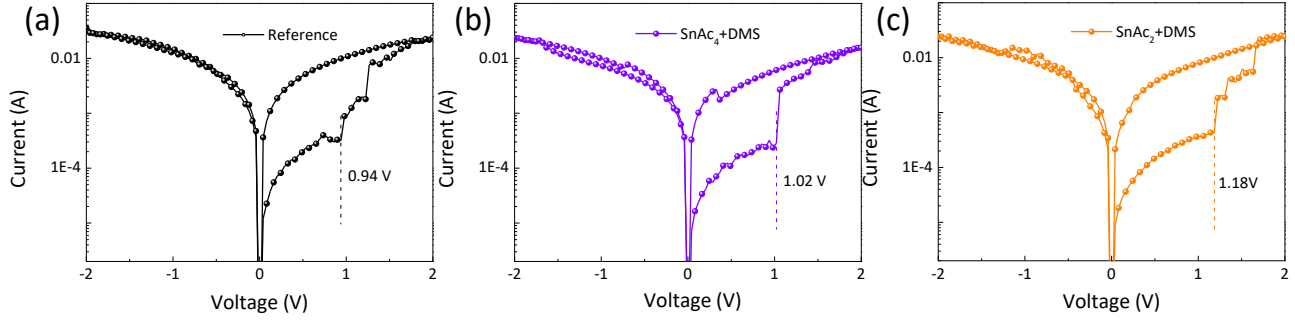


Figure 5 Typical J-V curves of reference (a), SnAc₄+DMS (b), and SnAc₂+DMS (c)-treated memory devices.

Grazing-incidence wide-angle X-ray scattering (GIWAXS) measurements are conducted to investigate the film structure and the crystalline orientation in the thin film. The GIWAXS patterns were recorded with incident angles of 0.5° (**Figure 3d-f**) and 2° (Figure S11) to probe the structure of the surface and the bulk region of the films, respectively. GIWAXS images taken in the surface region (Figure 3d-f) reveal the presence of both low dimensional and 3D-like crystallites. Full peak assignment is reported in Figure S10 and S12. The GIWAXS peak located at $q_z \sim 0.38 \text{ nm}^{-1}$ for the reference film indicates the presence of low dimensional crystallites with $n = 3$. When the film is treated with SnAc₄+DMS and SnAc₂+DMS, the low dimensional phase is fully transformed to $n = 5$ (see Figure S10 and S11d). In all films, the low dimensional phases are concentrated at the top portion of the perovskite film, indicating that a gradient structure of the quasi-2D perovskite is obtained, which is beneficial to protect it from the interaction with water and oxygen.⁴² The high angle signals in the GIWAXS patterns can be assigned to the presence of 3D-like crystallites with cubic structure.⁴⁹ The 3D-like crystallites present some degree of preferential orientation with crystals oriented both with the (111) and (100) planes parallel to the substrate (Figure S11). In these films produced by the two-step blade-coating procedure the (111) orientation seems to be dominant, in contrast to what previously observed on similar systems produced by a single-step spin-coating method.⁵⁰ The degree of alignment measurement for the 3D crystals is similar in all the prepared films. In agreement with SEM observations, GIWAXS patterns reveal the presence of highly aligned residual SnI₂/PbI₂ crystallites for the reference film. Interestingly, when the surface passivation is performed with SnAc₄+DMS, the residual SnI₂/PbI₂ crystallites diminish sensibly, and they disappear completely when the film is treated with SnAc₂+DMS (see Figure S10e), indicating that the surface treatment is re-crystallizing the top surface of the perovskite. The removal of SnI₂/PbI₂ precursor upon surface treatment is also confirmed by XRD (Figure S13), where the increase of the perovskite structural diffraction peaks indicates an enhanced crystallization upon surface treatment. In summary, our combined microscopy and X-ray analysis demonstrates how the two-step blade coating method, followed by a post-deposited chemical passivation allows to obtain dense films of textured 3D-like crystals without residual SnI₂/PbI₂ crystals, resulting a decrease of the surface traps.

Steady-state photoluminescence (PL) and time-resolved PL (TRPL) are reported in **Figure 4a** and S13-14. The reference sample exhibits lower emission intensity compared to the SnAc₂+DMS sample, implying higher nonradiative recombination associated with traps.⁵¹ This is supported by the faster decay dynamics of τ_{avg} of 42.47 ns versus 105.69 ns of the reference and SnAc₂+DMS treated samples, respectively (Table S4). These observations are well in line with the improvement in V_{OC} observed in devices. We also observe a slight blue shift of the PL peaks from 1.26 eV to 1.30 eV in conjunction with a reduced full width half maximum (FWHM) for the surface treated samples, which could also be attributed to the reduced number of traps states. To better understand the mechanism behind the significant improvement of V_{OC} , a Mott-Schottky plot analysis is conducted and shown in **Figure 4b**. The modified devices exhibit enhanced built-in potential (V_{bi}) of 0.81 V (SnAc₂+DMS) and 0.68 V (SnAc₄+DMS) compared to 0.60 V for the reference sample, resulting in an improved V_{OC} .⁵¹ **Figure 4c** shows the Nyquist plots of the three devices. The insert is the equivalent circuit for fitting the impedance spectroscopy (EIS) data, which consist of the series resistance (R_s), the bulk charge carrier recombination (capacitance C_1 and recombination resistance R_1), and the interfacial charge recombination (capacitance C_2 and recombination resistance R_2). A second semicircle is observed at low frequency for the reference and SnAc₄+DMS treated samples. The absence of the second semicircle in SnAc₂+DMS devices demonstrates efficient charge transfer at the perovskite/ETL contact interface after SnAc₂+DMS treatment. Moreover, a much higher recombination resistance is observed for SnAc₂+DMS treated device compared to the reference and SnAc₄+DMS in EIS measurement, indicating efficient passivation and suppression of carrier recombination with SnSe. The dark J-V curves of the three devices show similar diode behaviour, as shown in **Figure 4d**, but the lowest leakage current density for the SnAc₂+DMS treated sample further indicates that the in-situ generated SnSe plays an important role not only in reducing trap-induced recombination but also avoiding leakage. A similar conclusion can be drawn from the space charge limited current (SCLC) investigated with the device structure Au/perovskite/passivation layer/Au.⁵² As shown in Figure S15, measurements were conducted at scan speed of 1 mV/s with negligible transient ion diffusion, where the trap-filled limit voltage (V_{TFL}) decreases from 0.60 V for the reference device to 0.53 V

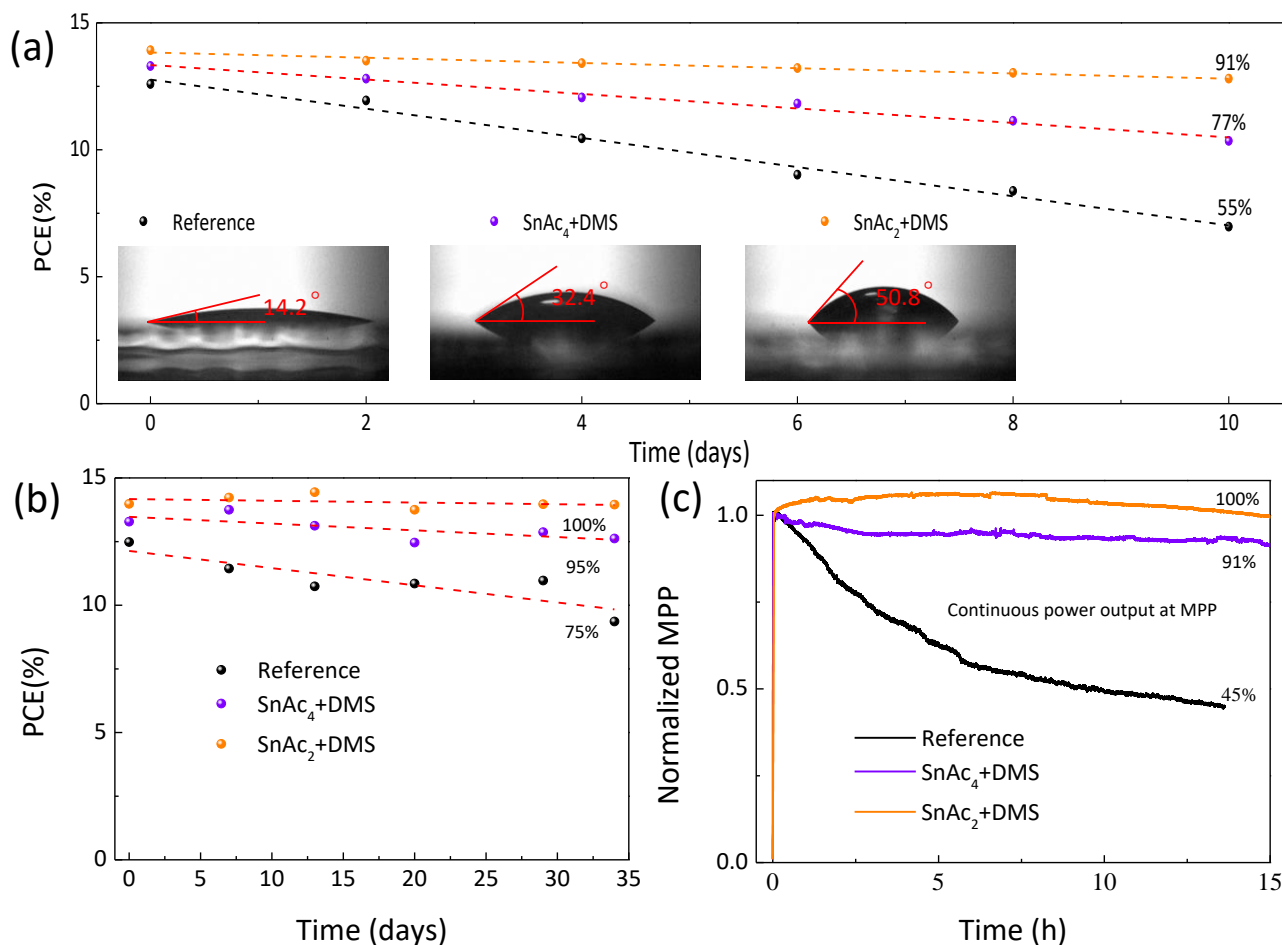


Figure 6 (a) Air stability (30%-40% humidity) of non-encapsulated quasi-2D Pb-Sn solar cells, the insert shows the contact angle of three corresponding active layer with passivation. Storage stability (b) and operational stability (c) of non-encapsulated devices in a N₂-filled glovebox. The operational stability is measured at the MPP under continuous 1 sun, AM1.5G illumination.

and 0.45 V for SnAc₄+DMS and SnAc₂+DMS treated devices, respectively. Therefore, all the experimental evidence shows that the suppressed trap-induced recombination at the contact interlayer with SnAc₂+DMS is at the origin of the high-performance devices.

It has been proposed by many that the surface traps in perovskites easily introduce ion mobility channels, which play a crucial role in device degradation.⁵³ It has also been demonstrated that halide ions migration under an electric field is one of the mechanisms for perovskite memory devices, therefore, we design a resistive random-access memory device to study the trap-induced ion migration behaviors with and without (w/wo) surface treatment.⁵⁴ Figure S16 reports the memory device structure of ITO/PEDOT:PSS/Quasi-2D Pb-Sn perovskite/(w/wo) passivation layer/Au, which works by switching the resistance of the perovskites between a high resistance state (HRS) and a low resistance state (LRS). J-V curves are measured at DC voltage (0 → 2 → 0 → -2 → 0 V) with rate of 0.04 V/s under dark condition. As the applied voltage increases from 0 to 2 V, the resistance changes from the HRS to the LRS at a well-defined voltage, as shown in **Figure 5a-c** by the dashed line. This transition voltage represents the barrier for halide ion migration, the large density of traps for the reference device led to a lower transition voltage of 0.94 V compared to 1.02 V of SnAc₄+DMS and 1.18 V for the SnAc₂+DMS treated samples. This memristor behavior represents a further demonstration that the in-situ passivation of SnSe plays a vital role in suppressing surface traps.

The reduced number of surface traps also plays an important role in enhancing the solar cell stability.⁵⁵ As shown in **Figure 6a**, the non-encapsulation quasi-2D Pb-Sn PSCs with SnAc₂+DMS retain 91% of initial PCE after aging in air (30%-40% humidity) for 10 days, while only 55% for reference and 77% for the SnAc₄+DMS sample is maintained under the same conditions. This is further verified by the lower number of pinholes and brighter regions (PbI₂/SnI₂) after storage in air, as shown by SEM micrographs (Figure S17). The insert shows the contact angle of the three corresponding films, highlighting that the surface treatment with SnAc₂+DMS creates a more hydrophobic surface due to the hydrophobic property of SnSe. Moreover, the non-encapsulated reference PSCs stored for one month in air (humidity 30%-40%) clearly shows visible degradation (Figure S17-18), which is absent for the treated samples. When devices are tested in a N₂-filled glovebox, the SnAc₂+DMS treated one shows nearly zero-degradation of the PCE

for over one month, while the SnAc₄+DMS and reference samples are degraded by 5% and 25%, respectively (**Figure 6b**). Naturally, the operational stability under AM 1.5 G standard spectrum is more important for solar cells. As shown in **Figure 6c**, the reference device lost over 50% after MPP tracking for 15 hours owing to light-accelerated ion migration, whereas PSCs with SnAc₄+DMS and SnAc₂+DMS retain 91% and 100% of their initial value, respectively. Therefore, we show that our surface treatment is an effective strategy and promising approach for improving device performance towards industrial standard.

Conclusions

In conclusion, a quasi-2D Pb-Sn perovskite of composition PEA₂(FA_{0.5}MA_{0.5})₄(Pb_{0.5}Sn_{0.5})₅l₁₆ with gradient structure is for the first time successfully prepared with a two-step blade coating. An in-situ reaction method is proposed to further reduce the number of surface traps. We compared two different surface treatments utilizing SnAc₂+DMS and SnAc₄+DMS, and we demonstrate the in-situ synthesis of SnSe on the perovskite surface by using SnAc₂+DMS. The sample with SnSe exhibits a reduced trap density and decreased nonradiative recombination losses. Therefore, we display a record PCE of 15.06% with a V_{OC} of 0.855 V, which are very significant improvements respect to the reference device (PCE of 12.42%, V_{OC} of 0.812 V) and the sample using SnAc₄+DMS (PCE of 13.65%, V_{OC} of 0.812 V) for which SnSe formation is not observed. It is important to stress that the hydrophobic SnSe significantly reduces the interaction with ambient gases. Therefore, the PSCs treated with SnAc₂+DMS showed remarkable environmental stability and operational stability, retaining 91% of the initial PCE after 10 days in ambient air (30%-40% humidity) without encapsulation, and showing nearly no-degradation of the PCE for either storage in a glovebox over one month or under continuous MPP tracking for 15 h. We believe these results pave the way for the development of stable and environmentally friendly perovskite devices.

Author contributions

L. Chen was responsible for device fabrication and measurement as well as the writing of the manuscript. E. K. Tekelenburg helped the Raman measurements as well as the PL studies. K. Gahlot, A. Lasorsa, L. Protesescu, and P.C.A. Van der Wel conducted the NMR experiments and analysed the data. M. Pitaro assisted with SEM measurement. K. Gahlot and L. Protesescu also assisted with the FTIR experiments and helped edit the manuscript. J. Xi measured and helped interpret the UPS data. G. Portale helped measure and analyze the GIWAXS data. C.J. Brabec helped improve data analysis of the entire manuscript. Giovanna Feraco and Petra Rudolf conducted the XPS measurement and analysis. M. A. Loi supervised the project, assisted with the writing of the manuscript. All authors commented on the manuscript.

Conflicts of interest

There are no conflicts to declare.

Acknowledgements

The authors thank the kind technical support of Arjen Kamp, Teo Zaharia, and Lorenzo Di Mario. L. Chen acknowledges the China Scholarship Council. This publication is part of the Netherlands Organization of Scientific Research (NWO) – Focus Group “Next Generation Organic Photovoltaics”, participating in the Dutch Institute for Fundamental Energy Research (DIFFER) and CogniGron research center. This work was partially funded by the European Union’s Horizon 2020 program, through a FET Proactive research and innovation action under grant agreement No. 101084124 (DIAMOND). J. Xi acknowledges the National Natural Science Foundation of China (Grant No. 62205264), and Xi'an Jiaotong University Young Talents Support Program (11302291010704).

References

1. O. Almora, D. Baran, G. C. Bazan, C. Berger, C. I. Cabrera, K. R. Catchpole, S. Erten - Ela, F. Guo, J. Hauch, A. W. Y. Ho - Baillie, T. J. Jacobsson, R. A. J. Janssen, T. Kirchartz, N. Kopidakis, Y. Li, M. A. Loi, R. R. Lunt, X. Mathew, M. D. McGehee, J. Min, D. B. Mitzi, M. K. Nazeeruddin, J. Nelson, A. F. Nogueira, U. W. Paetzold, N. G. Park, B. P. Rand, U. Rau, H. J. Snaith, E. Unger, L. Vaillant - Roca, H. L. Yip and C. J. Brabec, *Advanced Energy Materials*, 2021, **11**, 2102526.
2. L. Xiao, T. An, C. Deng, X. Xu and H. Sun, *Energy & Environmental Science*, 2023, DOI: 10.1039/d2ee02510h.
3. D. Zhao, Y. Yu, C. Wang, W. Liao, N. Shrestha, C. R. Grice, A. J. Cimaroli, L. Guan, R. J. Ellingson, K. Zhu, X. Zhao, R.-G. Xiong and Y. Yan, *Nature Energy*, 2017, **2**, 17018.

4. M. T. Klug, R. L. Milot, J. B. Patel, T. Green, H. C. Sansom, M. D. Farrar, A. J. Ramadan, S. Martani, Z. Wang, B. Wenger, J. M. Ball, L. Langshaw, A. Petrozza, M. B. Johnston, L. M. Herz and H. J. Snaith, *Energy & Environmental Science*, 2020, **13**, 1776-1787.
5. R. Lin, J. Xu, M. Wei, Y. Wang, Z. Qin, Z. Liu, J. Wu, K. Xiao, B. Chen, S. M. Park, G. Chen, H. R. Atapattu, K. R. Graham, J. Xu, J. Zhu, L. Li, C. Zhang, E. H. Sargent and H. Tan, *Nature*, 2022, **603**, 73-78.
6. J. Wang, M. A. Uddin, B. Chen, X. Ying, Z. Ni, Y. Zhou, M. Li, M. Wang, Z. Yu and J. Huang, *Advanced Energy Materials*, 2023, **13**.
7. G. Kapil, T. Bessho, Y. Sanehira, S. R. Sahamir, M. Chen, A. K. Baranwal, D. Liu, Y. Sono, D. Hirotsu, D. Nomura, K. Nishimura, M. A. Kamarudin, Q. Shen, H. Segawa and S. Hayase, *ACS Energy Letters*, 2022, **7**, 966-974.
8. J. Cao, H. L. Loi, Y. Xu, X. Guo, N. Wang, C. K. Liu, T. Wang, H. Cheng, Y. Zhu, M. G. Li, W. Y. Wong and F. Yan, *Adv Mater*, 2022, **34**, e2107729.
9. H. Liu, L. Wang, R. Li, B. Shi, P. Wang, Y. Zhao and X. Zhang, *ACS Energy Letters*, 2021, **6**, 2907-2916.
10. S. Shao and M. A. Loi, *Advanced Energy Materials*, 2021, **11**, 2003907.
11. M. Pitaro, E. K. Tekelenburg, S. Shao and M. A. Loi, *Adv Mater*, 2022, **34**, e2105844.
12. H. Kim, J. W. Lee, G. R. Han, S. K. Kim and J. H. Oh, *Advanced Functional Materials*, 2020, **31**, 2008801.
13. C. Li, R. Ma, X. He, T. Yang, Z. Zhou, S. Yang, Y. Liang, X. W. Sun, J. Wang, Y. Yan and W. C. H. Choy, *Advanced Energy Materials*, 2020, **10**, 1903013.
14. J. Werner, T. Moot, T. A. Gossett, I. E. Gould, A. F. Palmstrom, E. J. Wolf, C. C. Boyd, M. F. A. M. van Hest, J. M. Luther, J. J. Berry and M. D. McGehee, *ACS Energy Letters*, 2020, **5**, 1215-1223.
15. T. Jiang, Z. Chen, X. Chen, X. Chen, X. Xu, T. Liu, L. Bai, D. Yang, D. Di, W. E. I. Sha, H. Zhu and Y. M. Yang, *ACS Energy Letters*, 2019, **4**, 1784-1790.
16. C. Li, Y. Pan, J. Hu, S. Qiu, C. Zhang, Y. Yang, S. Chen, X. Liu, C. J. Brabec, M. K. Nazeeruddin, Y. Mai and F. Guo, *ACS Energy Letters*, 2020, **5**, 1386-1395.
17. W. Ke, C. Chen, I. Spanopoulos, L. Mao, I. Hadar, X. Li, J. M. Hoffman, Z. Song, Y. Yan and M. G. Kanatzidis, *Journal of the American Chemical Society*, 2020, **142**, 15049-15057.
18. J. Wang, K. Datta, J. Li, M. A. Verheijen, D. Zhang, M. M. Wienk and R. A. J. Janssen, *Advanced Energy Materials*, 2020, **10**, 2000566.
19. S. Hu, K. Otsuka, R. Murdey, T. Nakamura, M. A. Truong, T. Yamada, T. Handa, K. Matsuda, K. Nakano, A. Sato, K. Marumoto, K. Tajima, Y. Kanemitsu and A. Wakamiya, *Energy & Environmental Science*, 2022, **15**, 2096.
20. R. Prasanna, T. Leijtens, S. P. Dunfield, J. A. Raiford, E. J. Wolf, S. A. Swifter, J. Werner, G. E. Eperon, C. de Paula, A. F. Palmstrom, C. C. Boyd, M. F. A. M. van Hest, S. F. Bent, G. Teeter, J. J. Berry and M. D. McGehee, *Nature Energy*, 2019, **4**, 939-947.
21. C. Katan, N. Mercier and J. Even, *Chem Rev*, 2019, **119**, 3140-3192.
22. S. Shao, J. Liu, G. Portale, H.-H. Fang, G. R. Blake, G. H. ten Brink, L. J. A. Koster and M. A. Loi, *Advanced Energy Materials*, 2018, **8**, 1702019.
23. H. Ren, S. Yu, L. Chao, Y. Xia, Y. Sun, S. Zuo, F. Li, T. Niu, Y. Yang, H. Ju, B. Li, H. Du, X. Gao, J. Zhang, J. Wang, L. Zhang, Y. Chen and W. Huang, *Nature Photonics*, 2020, **14**, 154-163.
24. J. Dong, S. Shao, S. Kahmann, A. J. Rommens, D. Hermida - Merino, G. H. ten Brink, M. A. Loi and G. Portale, *Advanced Functional Materials*, 2020, **30**, 2001294.
25. H. Lai, D. Lu, Z. Xu, N. Zheng, Z. Xie and Y. Liu, *Adv Mater*, 2020, **32**, e2001470.
26. W. Fu, H. Liu, X. Shi, L. Zuo, X. Li and A. K. Y. Jen, *Advanced Functional Materials*, 2019, **29**, 1900221.
27. N. Zhou, Y. Shen, L. Li, S. Tan, N. Liu, G. Zheng, Q. Chen and H. Zhou, *Journal of the American Chemical Society*, 2018, **140**, 459-465.
28. J. Xi, I. Spanopoulos, K. Bang, J. Xu, H. Dong, Y. Yang, C. D. Malliakas, J. M. Hoffman, M. G. Kanatzidis and Z. Wu, *Journal of the American Chemical Society*, 2020, **142**, 19705-19714.
29. X. Li, K. Li, B. Wang, X. Zhang, S. Yue, Y. Li, Q. Chen, S. Li, T. Yue, H. Zhou and Y. Zhang, *Advanced Functional Materials*, 2021, **31**, 2107675.
30. J. Liang, Z. Zhang, Q. Xue, Y. Zheng, X. Wu, Y. Huang, X. Wang, C. Qin, Z. Chen and C.-C. Chen, *Energy & Environmental Science*, 2022, **15**, 296-310.
31. J. Zhang, J. Qin, M. Wang, Y. Bai, H. Zou, J. K. Keum, R. Tao, H. Xu, H. Yu, S. Haacke and B. Hu, *Joule*, 2019, **3**, 3061-3071.
32. X. Lian, H. Wu, L. Zuo, G. Zhou, X. Wen, Y. Zhang, G. Wu, Z. Xie, H. Zhu and H. Chen, *Advanced Functional Materials*, 2020, **30**, 2004188.
33. Z. Wang, Q. Wei, X. Liu, L. Liu, X. Tang, J. Guo, S. Ren, G. Xing, D. Zhao and Y. Zheng, *Advanced Functional Materials*, 2020, **31**, 2008404.
34. Y. Huang, Y. Li, E. L. Lim, T. Kong, Y. Zhang, J. Song, A. Hagfeldt and D. Bi, *Journal of the American Chemical Society*, 2021, **143**, 3911-3917.
35. P. Liu, N. Han, W. Wang, R. Ran, W. Zhou and Z. Shao, *Adv Mater*, 2021, **33**, e2002582.
36. Y. Zhang and N.-G. Park, *ACS Energy Letters*, 2022, **7**, 757-765.
37. Y. Chen, Y. Sun, J. Peng, P. Chabera, A. Honarfar, K. Zheng and Z. Liang, *ACS Appl Mater Interfaces*, 2018, **10**, 21343-21348.
38. Y. Wang, X. Lin, R. Zhou, T. Chen, Q. Lou, Q. Li and H. Zhou, *Advanced Photonics Research*, 2022, **3**, 2200079.
39. D. Ramirez, K. Schutt, Z. Wang, A. J. Pearson, E. Ruggeri, H. J. Snaith, S. D. Stranks and F. Jaramillo, *ACS Energy Letters*, 2018, **3**, 2246-2251.
40. J. Xi, H. Duim, M. Pitaro, K. Gahlot, J. Dong, G. Portale and M. A. Loi, *Advanced Functional Materials*, 2021, **31**, 2105734.
41. X. Li, W. Zhang, X. Guo, C. Lu, J. Wei and J. Fang, *Science*, 2022, **375**, 434.
42. J. Lu, T. Yang, T. Niu, N. Bu, Y. Zhang, S. Wang, J. Fang, X. Chang, T. Luo, J. Wen, Y. Yang, Z. Ding, K. Zhao and S. Liu, *Energy & Environmental Science*, 2022, **15**, 1144-1155.

43. B. Li, H. Di, B. Chang, R. Yin, L. Fu, Y. N. Zhang and L. Yin, *Advanced Functional Materials*, 2021, **31**, 2007447.
44. Y. Su, J. Yang, G. Liu, W. Sheng, J. Zhang, Y. Zhong, L. Tan and Y. Chen, *Advanced Functional Materials*, 2021, **32**, 2109631.
45. S. Yu, M. Abdellah, T. Pullerits, K. Zheng and Z. Liang, *Advanced Functional Materials*, 2021, **31**.
46. J. Zhang, H. Zhu, X. Wu, H. Cui, D. Li, J. Jiang, C. Gao, Q. Wang and Q. Cui, *Nanoscale*, 2015, **7**, 10807-10816.
47. V. R. Minnam Reddy, S. Gedi, B. Pejja and C. Park, *Journal of Materials Science: Materials in Electronics*, 2016, **27**, 5491-5508.
48. S. Shao, M. Abdu-Aguye, T. S. Sherkar, H.-H. Fang, S. Adjokatse, G. t. Brink, B. J. Kooi, L. J. A. Koster and M. A. Loi, *Advanced Functional Materials*, 2016, **26**, 8094-8102.
49. S. Kahmann, Z. Chen, O. Hordiichuk, O. Nazarenko, S. Shao, M. V. Kovalenko, G. R. Blake, S. Tao and M. A. Loi, *ACS Appl Mater Interfaces*, 2022, **14**, 34253-34261.
50. M. Pitaro, R. Pau, H. Duim, M. Mertens, W. T. M. Van Gompel, G. Portale, L. Lutsen and M. A. Loi, *Applied Physics Reviews*, 2022, **9**, 021407.
51. S. Shao, Y. Cui, H. Duim, X. Qiu, J. Dong, G. H. Ten Brink, G. Portale, R. C. Chiechi, S. Zhang, J. Hou and M. A. Loi, *Adv Mater*, 2018, **30**, e1803703.
52. L. Chen, Z. Yin, S. Mei, X. Xiao and H.-Q. Wang, *Journal of Power Sources*, 2021, **499**, 229909.
53. D. Meggiolaro, E. Mosconi and F. De Angelis, *ACS Energy Letters*, 2019, **4**, 779-785.
54. Y. Shao, Y. Fang, T. Li, Q. Wang, Q. Dong, Y. Deng, Y. Yuan, H. Wei, M. Wang, A. Gruverman, J. Shield and J. Huang, *Energy & Environmental Science*, 2016, **9**, 1752-1759.
55. S. Yang, S. Chen, E. Mosconi, Y. Fang, X. Xiao, C. Wang, Y. Zhou, Z. Yu, J. Zhao, Y. Gao, F. D. Angelis and J. Huang, *Science*, 2019, **365**, 473-478.¹